



# Formation of $\text{Li}_2\text{MnO}_3$ investigated by *in situ* synchrotron probes



Yongchun Kan<sup>a,b</sup>, Yuan Hu<sup>a</sup>, Jason Croy<sup>b</sup>, Yang Ren<sup>c</sup>, Cheng-Jun Sun<sup>c</sup>, Steve M. Heald<sup>c</sup>, Javier Bareño<sup>b</sup>, Ira Bloom<sup>b</sup>, Zonghai Chen<sup>b,\*</sup>

<sup>a</sup>State Key Laboratory of Fire Science, University of Science and Technology of China, Hefei, Anhui 230026, PR China

<sup>b</sup>Chemical Sciences and Engineering Division, Argonne National Laboratory, Argonne, IL 60439, USA

<sup>c</sup>X-ray Science Division, Argonne National Laboratory, Argonne, IL 60439, USA

## HIGHLIGHTS

- Formation of  $\text{Li}_2\text{MnO}_3$  was investigated by *in situ* high-energy X-ray diffraction and *in situ* X-ray absorption spectroscopy.
- An intermediate phase ( $\text{MnO}_2$ ) was captured by combining X-ray absorption spectroscopy and factor analysis techniques.
- Crystallization of  $\text{Li}_2\text{MnO}_3$  during sintering above 600 °C is anisotropic.

## ARTICLE INFO

### Article history:

Received 21 April 2014

Accepted 9 May 2014

Available online 16 May 2014

### Keywords:

*In situ* probes

XRD

XANES

Factor analysis

Lithium battery

## ABSTRACT

Both *in situ* high-energy X-ray diffraction and *in situ* X-ray absorption spectroscopy were used to investigate the structural evolution of materials during the solid-state synthesis of  $\text{Li}_2\text{MnO}_3$ . Combining X-ray absorption spectroscopy and factor analysis techniques, we were able to capture the spectrum and evolution of an intermediate phase ( $\text{MnO}_2$ ) that could not be detected by the diffraction technique. Meanwhile, the X-ray diffraction data clearly showed the anisotropic crystallization of  $\text{Li}_2\text{MnO}_3$  during sintering above 600 °C.

© 2014 Elsevier B.V. All rights reserved.

## 1. Introduction

Lithium cobalt oxide ( $\text{LiCoO}_2$ ) has been the dominant cathode material since its introduction in the first commercial lithium-ion cells in the early 1990s, which were used to power consumer electronics. Modern portable electronics and emerging technologies for electric vehicle (EV) applications have substantially raised expectations with regard to energy density, cost, safety, and life of available lithium-ion chemistries. To maintain structural integrity and good electrochemical performance,  $\text{Li}_{1-x}\text{CoO}_2$  can only reversibly utilize 50% of its lithium inventory (e.g.,  $0 \leq x \leq 0.5$ ) [1,2]. As repeatedly demonstrated in the open literature, the degree of lithium utilization can be significantly improved by replacing Co with other elements like Ni, Mn, and Li [3–9]. In particular, a high lithium utilization (close to  $x = 1$ ) was achieved for lithium-and-manganese-rich, nickel manganese cobalt oxides (LMR-NMC) while maintaining a good capacity retention [7,8]. In general, the

compositions of lithium transition metal oxides ( $\text{LiTMO}_2$ , TM = Ni, Mn, and Co) can be tuned such that Mn takes on an average 4+ oxidation state; this portion of Mn doesn't change its valence state during the normal charge/discharge operations of lithium-ion cells and, hence, improves the structural stability of cathode materials at higher degrees of lithium utilization. In LMR-NMC, excess Li and tetravalent Mn have a tendency to segregate and charge order into a honeycomb ( $\sqrt{3} \times \sqrt{3}$  superstructure) in the TM plane of the parent layered structure [10–14]. The resulted cation configuration can be regarded as an integrated structure containing both  $\text{Li}_2\text{MnO}_3$ - and  $\text{LiTMO}_2$ -like regions within the common close-packed oxygen lattice [7,9,13–15]. It is the presence of the electrochemically active  $\text{Li}_2\text{MnO}_3$  component that leads to the high reversible capacity of LMR-NMC [9]. However, the lack of understanding on the structure and the origin of the electrochemical activity of the  $\text{Li}_2\text{MnO}_3$  component represents a barrier that hinders the development of reliable LMR-NMC materials with high energy density for commercial applications [16,17]. Likewise, charge compensation mechanisms at play in a simpler, pure  $\text{Li}_2\text{MnO}_3$  system are not yet understood.

\* Corresponding author.

E-mail address: [zonghai.chen@anl.gov](mailto:zonghai.chen@anl.gov) (Z. Chen).

The unresolved issues for pure  $\text{Li}_2\text{MnO}_3$  are the lack of knowledge of (1) the charge compensation mechanisms related to electrochemical lithium extraction/insertion and (2) the complicated crystal structure and defects in  $\text{Li}_2\text{MnO}_3$ . Numerous research groups have reported  $\text{Li}_2\text{MnO}_3$  to be a promising cathode material for lithium-ion batteries that can deliver an initial charge capacity of more than  $250 \text{ mAh g}^{-1}$  [18–25]. However, the charge compensation mechanism that enables the extraction of lithium from  $\text{Li}_2\text{MnO}_3$  is still under intense debate. During the initial charge of  $\text{Li}_2\text{MnO}_3$ , there are four possible charge compensation mechanisms to balance the loss of lithium: (1) oxidation of manganese to form  $\text{Mn}^{\delta+}$  ( $\delta > 4$ ), [26] (2) evolution of oxygen ( $\text{O}_2$ ), [27,28] (3) partial oxidation of  $\text{O}^{2-}$  to  $\text{O}^-$ , [18,29,30] and (4) the ion exchange between  $\text{Li}^+$  and  $\text{H}^+$  [31,32]. The mechanism of oxidizing  $\text{Mn}^{4+}$  is the least attractive because it is generally believed hard to oxidize Mn beyond  $4+$  in an octahedral oxygen environment, [31] and the conversion of  $\text{Mn}^{4+}$  to  $\text{Mn}^{\delta+}$  ( $\delta > 4$ ) has yet to be experimentally validated [33]. On the other hand, the hypothesis of oxygen evolution or ion exchange can explain the initial charge capacity of  $\text{Li}_2\text{MnO}_3$ , but encounters difficulty in accounting for the reversible charge/discharge capacity after the initial electrochemical activation. A prevailing hypothesis is that all four mechanisms contribute partially to the electrochemical activity of  $\text{Li}_2\text{MnO}_3$ , with a dominant contribution from the partial oxidation of  $\text{O}^{2-}$  into  $\text{O}^-$ , which allows for both the extraction and the back-insertion of lithium. Another difficulty for these charge compensation mechanisms is the strong kinetic dependence of the electrochemical activity on the size, crystallinity, and dopant in the defect-rich  $\text{Li}_2\text{MnO}_3$  [21,23–25,34–38]. It is believed that these charge-compensation mechanisms must be associated with a specific type of structural defect in  $\text{Li}_2\text{MnO}_3$  to enable reversible extraction and insertion of lithium. In this work, both *in situ* high-energy X-ray diffraction (HEXRD) and *in situ* X-ray absorption near edge spectroscopy (XANES) were applied to investigate the structure and defect evolution during the solid-state synthesis of  $\text{Li}_2\text{MnO}_3$ .

## 2. Experimental

### 2.1. Solid-state synthesis of $\text{Li}_2\text{MnO}_3$

$\text{MnCO}_3$  (Aldrich) and  $\text{Li}_2\text{CO}_3$  (Aldrich) with a molar ratio of 1:1.05 were mechanically mixed for 24 h. Separate batches of the mixed powder were then annealed, in air, at temperatures of 450–950 °C with a constant heating rate of  $5^\circ\text{C min}^{-1}$ . The samples were then annealed at specific temperatures, as noted in the text, for 10 h before being naturally cooled to room temperature (RT).

### 2.2. High resolution X-ray diffraction (HRXRD)

The HRXRD patterns of  $\text{Li}_2\text{MnO}_3$  samples synthesized at various temperatures were collected at sector 11-BM of the Advanced Photon Source (APS) at Argonne National Laboratory. The wavelength of the X-ray beam used was  $0.413326 \text{ \AA}$ . The diffraction peaks of  $\text{Li}_2\text{MnO}_3$  were indexed in both C2/m space and R-3m space in this work. Therefore, the notation for indexing will be  $(hkl)_R$  for indexing in R-3m space and  $(hkl)_C$  for indexing in C2/m space.

### 2.3. *In situ* HEXRD

The powder mixture of  $\text{MnCO}_3$  and  $\text{Li}_2\text{CO}_3$  was compressed into a pellet of about 2 mm in thickness. The pellet was then placed in a programmable furnace (Linkam TS 1500) vertically with the X-ray beam aiming at the center of the pellet. The sample was then heated from RT to 1000 °C with a constant heating rate of  $1^\circ\text{C min}^{-1}$ . The *in situ* HEXRD experiment was carried out at sector

11-ID-C of the APS. The wavelength of the X-ray beam was pre-fixed at  $0.10804 \text{ \AA}$ . During the *in situ* solid-state synthesis, a 2D X-ray detector was deployed to collect the XRD patterns at a rate of one spectrum per minute. The details of the experimental setup can be found in our previous report [39].

### 2.4. *In situ* XANES

A similar solid-state synthesis setup was also used for *in situ* XANES experiments, except that the thickness of the pellet was reduced to about 0.1 mm for full penetration of the incident X-ray beam through the sample. *In situ* XANES experiments were performed at the K-edge of Mn (in the range of 6387–6780 eV) to monitor the change of the chemical environment of Mn during the formation of  $\text{Li}_2\text{MnO}_3$  from  $\text{MnCO}_3$  and  $\text{Li}_2\text{CO}_3$ . XANES spectra were recorded *in situ* every 125 s in a transmission mode at beamline 20-BM of APS using a Si (111) monochromator. Energy calibration of each spectrum was performed by aligning the first derivative maximum of a reference Mn XANES spectrum, spectrum collected simultaneously from a Mn metal foil in the reference channel, to the literature value of 6537.67 eV.

### 2.5. Factor analysis

Factor analysis techniques were applied to analyze the evolution of Mn XANES spectra during the solid-state synthesis of  $\text{Li}_2\text{MnO}_3$ . The mathematical processing of the *in situ* XANES data consisted of three steps: (1) principal factor analysis (PCA), (2) evolving factor analysis (EFA), and (3) target transfer factor analysis (TTFA) [40].

The *in situ* XANES data were first assembled into a data matrix  $D$ . Each column of the matrix  $D$  represents the absorbance of X-rays at different wavelengths (or photon energy) of the incident X-ray beam, while each row represents an absorption spectrum at a fixed temperature (or experimental time). For the dataset in this work,  $D$  was a  $206 \times 167$  matrix. In the process of PCA, a singular vector decomposition (SVD) algorithm was applied to decompose the matrix  $D$  into three independent matrices where  $U$  and  $V$  are orthogonal matrices representing the abstract concentration profiles and spectra, respectively. The superscript  $T$  indicates the transpose matrix and  $S$  is a diagonal matrix. Each eigenvalue  $s_{ii}$  represents the statistical weight of (or information contributed by) the  $i$ -th abstract spectrum (eigenvector) of the decomposition.

$$[D] = [U][S][V]^T \quad (1)$$

Then, a mathematical indicator, cumulative percent variance (CPV), [41] is calculated by using Equation (2), which determines the number of independent eigenvectors (i.e., the number of distinguishable chemical species present,  $k$ ) necessary to describe the changes in Mn XANES spectra during the solid-state synthesis of  $\text{Li}_2\text{MnO}_3$ .

$$\text{CPV}(k) = \left( \frac{\sum_{i=1}^k s_{ii}}{\sum_{i=1}^N s_{ii}} \right) \times 100\% \quad (2)$$

In Equation (2),  $N (=167)$  is the number of spectra in the dataset and, by convention, the eigenvalues  $s_{ii}$  are ordered from greatest to lowest.

In this step, the number of independent eigenvectors ( $k$ ) can potentially be mathematically reduced for the following reasons: (1) indistinguishable concentration profiles when two or more chemical species have a fixed concentration ratio throughout the whole course of the experiment, and (2) indistinguishable spectra

when two or more chemical species have close or identical absorption spectra. The resulting first four CPV( $k$ ) values are: 77.2%, 97.1%, 99.0%, and 99.3%. Therefore, three eigenvectors (abstract profiles) are enough to account for 99% of the variance in the experimental profiles, while adding a fourth eigenvector to the basis set provides only a marginal improvement of the description. Next, a new data matrix was then constructed using only the first three pairs of eigenvalues and eigenvectors:

$$[D'] = [U'] [S'] [V']^T \quad (3)$$

EFA was performed to estimate the concentration profiles of each distinguishable chemical species during the experiment. The data matrix  $D$  was arbitrarily divided into two sub-matrices  $D^{\text{top}}$  and  $D^{\text{bottom}}$ ;  $D^{\text{top}}$  represents the upper part of the matrix, and  $D^{\text{bottom}}$  represents the remaining matrix below the division point. The SVD algorithm was applied to both  $D^{\text{top}}$  and  $D^{\text{bottom}}$  to obtain the first three major eigenvalues for each sub-matrix. The evolving eigenvalues for the top and bottom matrices are shown in Fig. 1a and b, respectively. When pairing the 1st set of eigenvalues for the top matrices (black squares in Fig. 1a) and the 3rd set of eigenvalues for the bottom matrices (blue triangles in Fig. 1b), the minimum of these two sets of eigenvalues gives the initial estimate of the abstract concentration profile of the first chemical species ( $\text{MnCO}_3$  for this study) (see Fig. 1c). The initial estimate of the concentration profile for the second chemical species can be obtained by pairing the 2nd set of eigenvalues of the top matrices with the 2nd set of eigenvalues of the bottom matrices. The initial estimate for the third chemical species can be obtained by pairing the 3rd set of eigenvalues of the top matrices with the 1st set of eigenvalues of the bottom matrices.

Finally, TTFA was applied to obtain the nominal concentration profiles of the distinguishable chemical species, as shown in Equation (4).

$$C = U' U'^T C_{\text{est}} \quad (4)$$

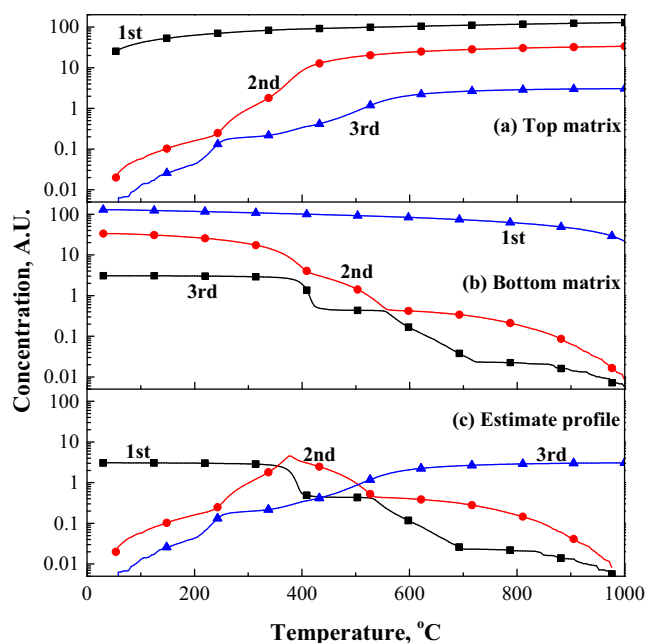


Fig. 1. Evolution of principal eigenvalues for (a) top matrix and (b) bottom matrix as functions of the dividing position and (c) projected concentration profiles of three distinguishable chemical species using EFA.

where  $C$  is the nominal concentration profiles without normalization for the distinguishable chemical species,  $U$  is the orthogonal eigenvectors obtained from the PCA process, and  $C_{\text{est}}$  is the initial estimate of the concentration profiles obtained from EFA. Then, the nominal absorption spectra profiles ( $S$ ) for each species can be obtained from Equation (5).

$$S = [C^T C]^{-1} C^T D' \quad (5)$$

### 3. Results and discussion

#### 3.1. In situ HEXRD

Fig. 2 shows the evolution of HEXRD patterns during the solid-state synthesis of  $\text{Li}_2\text{MnO}_3$  with a constant heating rate of  $1^\circ\text{C min}^{-1}$ . The peak positions of the characteristic reflections of  $\text{MnCO}_3$  and  $\text{Li}_2\text{CO}_3$  are labeled on the bottom of Fig. 2. No phase changes were observed at temperatures below  $369^\circ\text{C}$ , above which a new set of reflections corresponding to  $\text{Li}_2\text{MnO}_3$  appeared and their intensity increased with the heating temperature. The reflection peaks for  $\text{MnCO}_3$ , one of the raw materials, did not vanish until  $469^\circ\text{C}$ , while reflections from  $\text{Li}_2\text{CO}_3$  were visible up to  $729^\circ\text{C}$ . Since the structure and defect evolution of  $\text{Li}_2\text{MnO}_3$  were the focus of this work, both qualitative analysis and Rietveld refinement were carried out to obtain more information from HEXRD patterns above  $600^\circ\text{C}$ .

Fig. 3 shows a comparison of experimental (a) HRXRD and (b) HEXRD profiles and calculated XRD profiles from both (c) C2/m and (d) R-3m structures. The HEXRD pattern was obtained during the *in situ* experiment when the sample was heated to  $1000^\circ\text{C}$ , while the HRXRD pattern was collected at RT for  $\text{Li}_2\text{MnO}_3$  synthesized at  $850^\circ\text{C}$ . The model patterns were calculated based on the experimental cell parameters determined from the *in situ* HEXRD pattern at  $1000^\circ\text{C}$ . Therefore, the peaks in the HRXRD pattern are slightly shifted toward bigger  $1/d$  values due to the difference of the experimental temperature.

Highlighted with a dashed rectangle in Fig. 3 are the characteristic peaks of  $\text{Li}_2\text{MnO}_3$  revealing Li and Mn ordering in the TM layers; included are the  $(020)_c$ ,  $(110)_c$ , and  $(-111)_c$  peaks based on the monoclinic C2/m model, which are forbidden in the trigonal R-3m model. However, higher order super reflection peaks (e.g.,  $(221)_c$ ,  $(643)_c$ ,  $(-243)_c$ ,  $(152)_c$ ,  $(223)_c$ ,  $(-432)_c$ , and  $(-172)_c$  were absent from both the *in situ* HEXRD pattern and the *ex situ* HRXRD

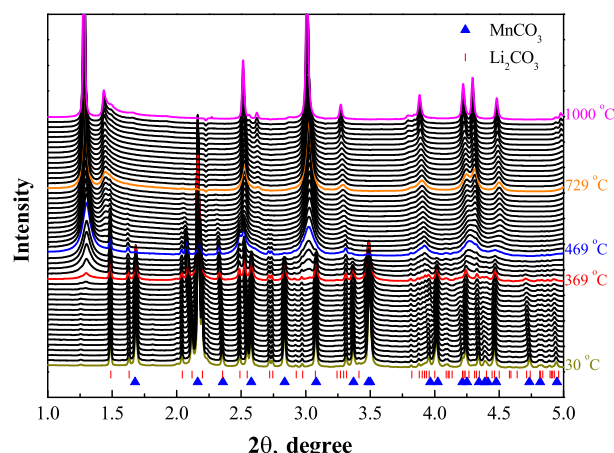


Fig. 2. Evolution of HEXRD profiles during solid-state synthesis of  $\text{Li}_2\text{MnO}_3$ .

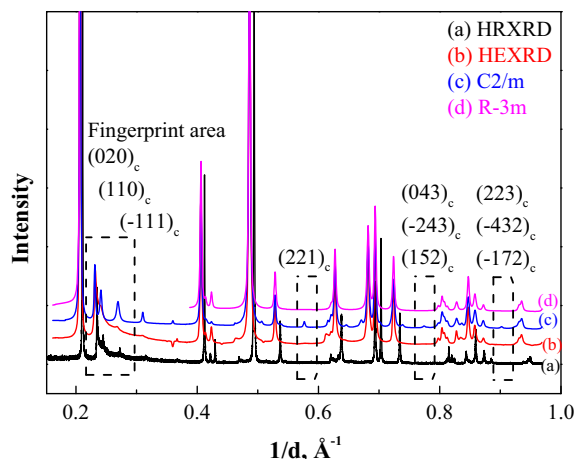


Fig. 3. A comparison of experimental XRD profiles and calculated XRD profiles for  $\text{Li}_2\text{MnO}_3$ , indicating a short-range ordering in  $\text{Li}_2\text{MnO}_3$ .

pattern, indicating that the absence of these peaks was not caused by insufficient annealing time, but originated from defects in Li–Mn ordering.

Excluding the monoclinic superreflections and using an R-3m structure model improves the quality of the Rietveld refinement of the data. Fig. 4a shows an example of such refinement of an HEXRD pattern acquired at 1000 °C. The same approach was applied for Rietveld refinement of all the HEXRD patterns collected within the temperature range between 600 °C and 1000 °C. As the temperature increases, Fig. 4b shows that the  $c$  value of the unit cell increased linearly with the  $a$  or  $b$  value. For the HEXRD patterns

shown in Fig. 4a, the  $(003)_R$  peak stems from cation segregation into pure Li and  $\text{Li}_{1/3}\text{Mn}_{2/3}$  cation sheets perpendicular to the  $c$ -axis, while the superreflections are due to the Li–Mn ordering within the  $\text{Li}_{1/3}\text{Mn}_{2/3}$  sheets. When the temperature was below 930 °C, the area of the  $(003)_R$  peak increased linearly with the peak area inside the fingerprint area (see Fig. 4c). A change on the trend was observed when the temperature was above 930 °C; the growing rate of  $(003)_R$  peak area was slower than that of the fingerprint area. The physical meaning of this transition point is not clear to us at the current state. It could correlate to the formation of spinel-like structures, as previously reported by Delmas et al. [38]. A second possibility is the decrease of the twin boundary on  $c$  axis. Structural modeling to investigate the impact of the  $\text{Li}_{1/3}\text{Mn}_{2/3}$  stacking sequence on the peak intensity is undergoing, and the results will be reported later. In addition, the heating process can lead to the increased crystallinity of  $\text{Li}_2\text{MnO}_3$ . Fig. 4d plots the full width at half maximum (FWHM) of the  $(003)_R$  peak as a function of the FWHM of the  $(110)_R$  peak. The figure shows that the FWHMs of both the  $(003)_R$  and the  $(110)_R$  peaks decrease steadily with the heating temperature, suggesting increased crystallinity. When the temperature was beyond 790 °C, the FWHM of the  $(003)_R$  peak decreased faster than that of the  $(110)_R$  peak, indicating a preferred crystallization along the  $c$ -axis that reduced the stacking faults or the micro-strain in that direction.

### 3.2. Ex situ HRXRD

To validate the structure/defect evolution of  $\text{Li}_2\text{MnO}_3$  at an equilibrium state,  $\text{Li}_2\text{MnO}_3$  powders were prepared by annealing the  $\text{MnCO}_3/\text{Li}_2\text{CO}_3$  mixtures at temperatures ranging from 450 °C to 850 °C. Fig. 5 shows the normalized HRXRD patterns for  $\text{Li}_2\text{MnO}_3$  powders synthesized at different temperatures; all the XRD

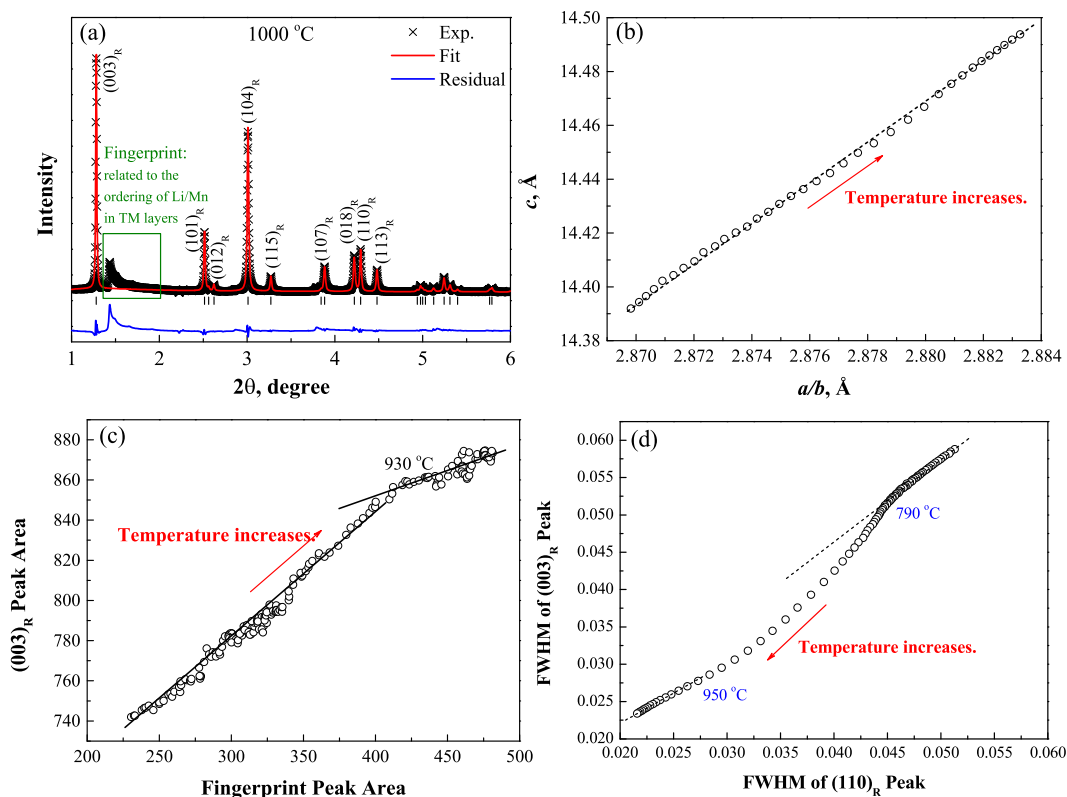


Fig. 4. (a) A typical fit of *in situ* HEXRD patterns (at 1000 °C) using a R-3m model, (b) evolution of cell parameters as functions of heating temperature, (c) a plot of the  $(003)_R$  peak area versus the integrate fingerprint area between 1.38° and 1.95°, and (d) evolution of the FWHM of the  $(003)_R$  and  $(110)_R$  peaks.



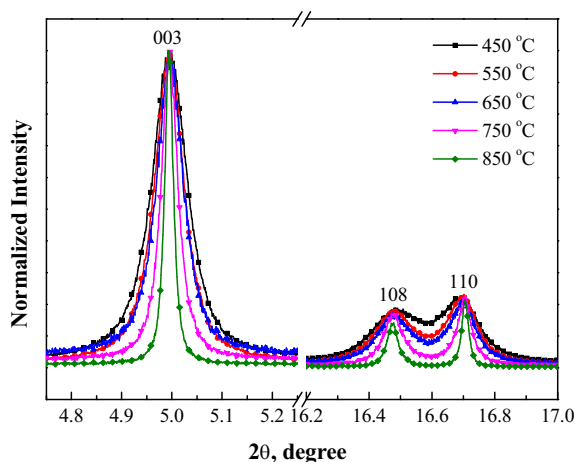


Fig. 5. Normalized HRXRD patterns for  $\text{Li}_2\text{MnO}_3$  powders synthesized at different temperatures.

patterns were normalized to the intensity of the  $(003)_R$  peak (or the  $(001)_c$  peak in the  $C2/m$  space) to clearly show the change of the peak width. It is clear that  $\text{Li}_2\text{MnO}_3$  synthesized at low temperature has poor crystallinity, where the HRXRD pattern features broadened peaks. As the annealing temperature increased, the diffraction peaks became sharper. Similar to what is shown in Fig. 3, the super reflection peaks for the  $C2/m$  structure at high angles were not observed for any of the samples. By excluding the data in the fingerprint area, we were able to fit all the HRXRD data with an R-3m model in which the TM layer is randomly occupied with  $1/3$  Li and  $2/3$  Mn (see Fig. 6 for a typical fitting). This suggests that defects in the  $ab$  plane, possibly the inter-exchange between Li and Mn, still existed for well-annealed samples.

### 3.3. *In situ* XANES

Fig. 7 shows the evolution of Mn K-edge XANES data during the solid-state synthesis of  $\text{Li}_2\text{MnO}_3$ . At the beginning of the experiment, X-ray absorption can be attributed to  $\text{MnCO}_3$ , one of the starting materials. No clear change of either the shape or the intensity of the absorption spectra was observed during the initial heating process up to  $290^\circ\text{C}$ , after which the major absorption peak shifted from  $6549\text{ eV}$  to  $6560\text{ eV}$ , consistent with oxidation of Mn.

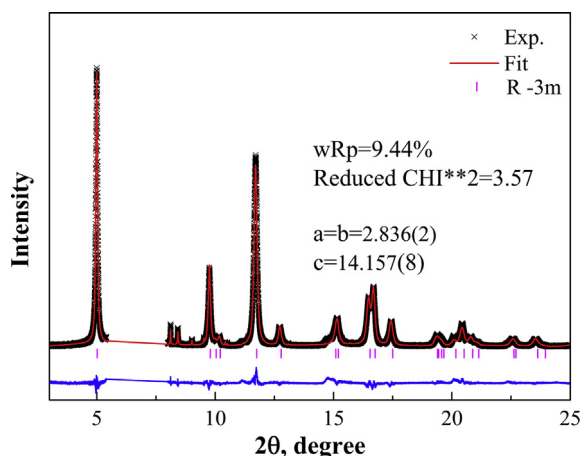


Fig. 6. A typical fit of *ex situ* HRXRD patterns for  $\text{Li}_2\text{MnO}_3$  synthesized at  $550^\circ\text{C}$  using an R-3m model.

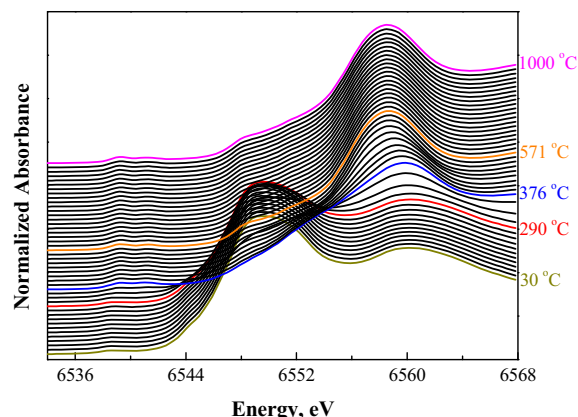


Fig. 7. Evolution of XANES profiles during the solid-state synthesis of  $\text{Li}_2\text{MnO}_3$ .

Above  $\sim 570^\circ\text{C}$ , the absorption peak shifted back to  $6558\text{ eV}$ , indicating a further change in oxidation state and/or coordination of Mn within the temperature range of  $376^\circ\text{C}$ – $571^\circ\text{C}$ . This observation indicates the presence of an intermediate Mn species during the solid-state reaction that was not captured by *in situ* HEXRD.

To reveal the detailed reaction pathway for solid-state synthesis of  $\text{Li}_2\text{MnO}_3$ , factor analysis techniques were applied to the *in situ* XANES data to obtain the absorption spectrum of the intermediate phase. The mathematical criterion CPV suggests that three independent vectors were needed to describe the data matrix from the *in situ* experiment (See Experimental Section for details). The *in situ* HEXRD data showed that the reaction started with  $\text{MnCO}_3$  and ended with  $\text{Li}_2\text{MnO}_3$ . It has to be noted that the CPV criterion to determine the dimensionality of the spectral series (number of abstract profiles present) is independent of the physical interpretation based on HEXRD data, therefore, providing evidence of the existence of just one intermediate.

Fig. 8a and b shows the concentration profiles and corresponding absorption spectra of the three distinguishable chemical species, which were calculated by using EFA and TTFA, with  $\text{MnCO}_3$  and  $\text{Li}_2\text{MnO}_3$  assigned based on the results of *in situ* HEXRD. Fig. 8b shows that the absorption edge of the intermediate phase is substantially higher than that of  $\text{MnCO}_3$ , but very close to that of  $\text{Li}_2\text{MnO}_3$ . The calculated spectrum of the intermediate phase is close to the measured spectrum of  $\delta\text{-MnO}_2$  by Gorlin et al. [42]. Therefore, the intermediate phase was assigned to  $\text{MnO}_2$ . Fig. 8a shows that the intermediate phase ( $\text{MnO}_2$ ) started to evolve at about  $200^\circ\text{C}$ , when the concentration of  $\text{MnCO}_3$  started to decrease; the concentration of  $\text{MnO}_2$  reached a maximum at about  $400^\circ\text{C}$ , when  $\text{MnCO}_3$  completely disappeared. After that,  $\text{MnO}_2$  reacted with  $\text{Li}_2\text{CO}_3$ , or  $\text{Li}_2\text{O}$  produced by the decomposition of  $\text{Li}_2\text{CO}_3$ , resulting in the reducing amounts of  $\text{Li}_2\text{CO}_3$  and  $\text{MnO}_2$  and the evolution of  $\text{Li}_2\text{MnO}_3$ . When the temperature was above  $600^\circ\text{C}$ , no new distinguishable chemical species were detected by factor analysis approaches, and no visible changes in the XANES data were found (Fig. 7). Thus, no major change in the local chemical environment for Mn was observed during the sintering process.

## 4. Conclusion

*In situ* HEXRD and *in situ* XANES were applied to trace the structure and defect evolution during the solid-state synthesis of  $\text{Li}_2\text{MnO}_3$ . The results indicate that the solid-state reaction forming  $\text{Li}_2\text{MnO}_3$  can be divided into four sequential stages: (1) decomposition of  $\text{MnCO}_3$  and formation of  $\text{MnO}_2$  within the temperature

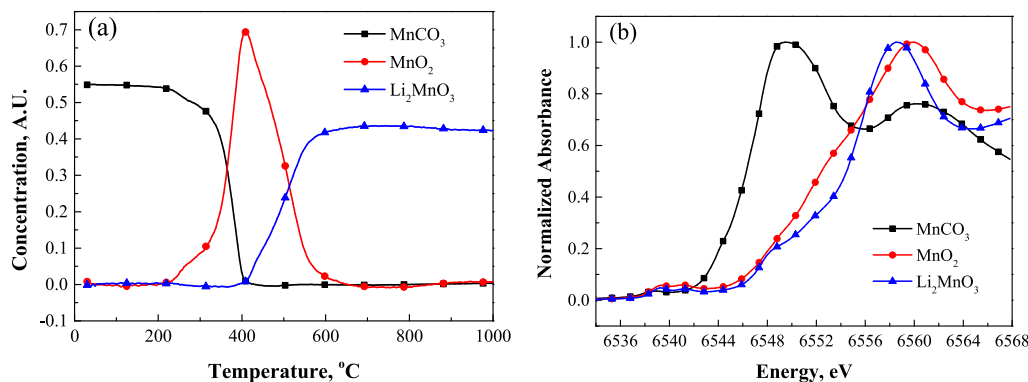


Fig. 8. (a) Calculated concentration profiles and (b) calculated absorption spectra for MnCO<sub>3</sub>, MnO<sub>2</sub>, and Li<sub>2</sub>MnO<sub>3</sub> during the solid-state reaction.

window between 200 °C and 400 °C; (2) reaction between MnO<sub>2</sub> and Li<sub>2</sub>CO<sub>3</sub> (or Li<sub>2</sub>O) to form Li<sub>2</sub>MnO<sub>3</sub>; (3) crystallization of Li<sub>2</sub>MnO<sub>3</sub> with a preference along the *c*-axis when the temperature is above 790 °C; and (4) inter-exchange of cations that possibly leads to the formation of spinel-like structures or a reduction of twin boundaries at above 900 °C. These findings also suggest that the type and the amount of defects in Li<sub>2</sub>MnO<sub>3</sub> can be actively controlled by the synthesis conditions of the solid-state reaction.

## Acknowledgments

Research at Argonne National Laboratory was funded by U.S. Department of Energy, Vehicle Technologies Office. Argonne National Laboratory is operated for the U.S. Department of Energy by UChicago Argonne, LLC, under contract DE-AC02-06CH11357. The authors also acknowledge the use of the Advanced Photon Source of Argonne National Laboratory supported by the U.S. Department of Energy, Office of Science, Office of Basic Energy Sciences. PNC/XSD facilities at the Advanced Photon Source, and research at these facilities, are supported by the US Department of Energy – Basic Energy Sciences, a Major Resources Support grant from NSERC, the University of Washington, the Canadian Light Source, and the Advanced Photon Source.

## References

- [1] Z.H. Chen, J.R. Dahn, *Electrochim. Acta* 49 (2004) 1079–1090.
- [2] Z.H. Chen, Z.H. Lu, J.R. Dahn, *J. Electrochem. Soc.* 149 (2002) A1604–A1609.
- [3] Y.K. Sun, Z.H. Chen, H.J. Noh, D.J. Lee, H.G. Jung, Y. Ren, S. Wang, C.S. Yoon, S.T. Myung, K. Amine, *Nat. Mater.* 11 (2012) 942–947.
- [4] Y.K. Sun, S.T. Myung, B.C. Park, J. Prakash, I. Belharouak, K. Amine, *Nat. Mater.* 8 (2009) 320–324.
- [5] Z.H. Lu, Z.H. Chen, J.R. Dahn, *Chem. Mater.* 15 (2003) 3214–3220.
- [6] Z.H. Lu, J.R. Dahn, *J. Electrochem. Soc.* 149 (2002) A815–A822.
- [7] D. Kim, G. Sandi, J.R. Croy, K.G. Gallagher, S.H. Kang, E. Lee, M.D. Slater, C.S. Johnson, M.M. Thackeray, *J. Electrochem. Soc.* 160 (2013) A31–A38.
- [8] J.R. Croy, S.H. Kang, M. Balasubramanian, M.M. Thackeray, *Electrochem. Commun.* 13 (2011) 1063–1066.
- [9] S.H. Park, S.H. Kang, C.S. Johnson, K. Amine, M.M. Thackeray, *Electrochem. Commun.* 9 (2007) 262–268.
- [10] J. Baren, C.H. Lei, J.G. Wen, S.H. Kang, I. Petrov, D.P. Abraham, *Adv. Mater.* 22 (2010) 1122–1127.
- [11] C.H. Lei, J.G. Wen, M. Sardela, J. Baren, I. Petrov, S.H. Kang, D.P. Abraham, *J. Mater. Sci.* 44 (2009) 5579–5587.
- [12] R. Wang, X.Q. He, L.H. He, F.W. Wang, R.J. Xiao, L. Gu, H. Li, L.Q. Chen, *Adv. Energy Mater.* 3 (2013) 1358–1367.
- [13] E. McCalla, C.M. Lowart, C.R. Brown, J.R. Dahn, *Chem. Mater.* 25 (2013) 912–918.
- [14] J. Breger, M. Jiang, N. Dupre, Y.S. Meng, Y. Shao-Horn, G. Ceder, C.P. Grey, *J. Solid State Chem.* 178 (2005) 2575–2585.
- [15] J. Baren, M. Balasubramanian, S.H. Kang, J.G. Wen, C.H. Lei, S.V. Pol, I. Petrov, D.P. Abraham, *Chem. Mater.* 23 (2011) 2039–2050.
- [16] J.R. Croy, K.G. Gallagher, M. Balasubramanian, Z.H. Chen, Y. Ren, D. Kim, S.H. Kang, D.W. Dees, M.M. Thackeray, *J. Phys. Chem. C* 117 (2013) 6525–6536.
- [17] K.G. Gallagher, J.R. Croy, M. Balasubramanian, M. Bettge, D.P. Abraham, A.K. Burrell, M.M. Thackeray, *Electrochem. Commun.* 33 (2013) 96–98.
- [18] M. Sathiy, K. Ramesha, G. Rousse, D. Foix, D. Gonbeau, A.S. Prakash, M.L. Doublet, K. Hemalatha, J.M. Tarascon, *Chem. Mater.* 25 (2013) 1121–1131.
- [19] M. Sathiy, G. Rousse, K. Ramesha, C.P. Laisa, H. Vezin, M.T. Sougrati, M.L. Doublet, D. Foix, D. Gonbeau, W. Walker, A.S. Prakash, M. Ben Hassine, L. Dupont, J.M. Tarascon, *Nat. Mater.* 12 (2013) 827–835.
- [20] D.Y.W. Yu, K. Yanagida, Y. Kato, H. Nakamura, *J. Electrochem. Soc.* 156 (2009) A417–A424.
- [21] M. Tabuchi, Y. Nabeshima, T. Takeuchi, K. Tatsumi, J. Imaizumi, Y. Nitta, *J. Power Sources* 195 (2010) 834–844.
- [22] K. Kubota, T. Kaneko, M. Hirayama, M. Yonemura, Y. Imanari, K. Nakane, R. Kanno, *J. Power Sources* 216 (2012) 249–255.
- [23] M. Tabuchi, A. Nakashima, H. Shigemura, K. Ado, H. Kobayashi, H. Sakaebe, H. Kageyama, T. Nakamura, M. Kohzaki, A. Hirano, R. Kanno, *J. Electrochem. Soc.* 149 (2002) A509–A524.
- [24] S. Kim, J.K. Noh, S. Yu, W. Chang, K.Y. Chung, B.W. Cho, *J. Electroceram.* 30 (2013) 159–165.
- [25] S.F. Amalraj, B. Markovsky, D. Sharon, M. Talianker, E. Zinigrad, R. Persky, O. Haik, J. Grinblat, J. Lampert, M. Schulz-Dobrick, A. Garsuch, L. Burlaka, D. Aurbach, *Electrochim. Acta* 78 (2012) 32–39.
- [26] P. Kalyani, S. Chitra, T. Mohan, S. Gopukumar, *J. Power Sources* 80 (1999) 103–106.
- [27] A.R. Armstrong, M. Holzapfel, P. Novak, C.S. Johnson, S.H. Kang, M.M. Thackeray, P.G. Bruce, *J. Am. Chem. Soc.* 128 (2006) 8694–8698.
- [28] H. Koga, L. Croguennec, M. Menetrier, P. Mannesiez, F. Weill, C. Delmas, *J. Power Sources* 236 (2013) 250–258.
- [29] R.J. Xiao, H. Li, L.Q. Chen, *Chem. Mater.* 24 (2012) 4242–4251.
- [30] H. Koga, L. Croguennec, M. Menetrier, K. Dohil, S. Belin, L. Bourgeois, E. Suard, F. Weill, C. Delmas, *J. Electrochem. Soc.* 160 (2013) A786–A792.
- [31] A.D. Robertson, P.G. Bruce, *Chem. Mater.* 15 (2003) 1984–1992.
- [32] A.D. Robertson, P.G. Bruce, *Chem. Commun.* (2002) 2790–2791.
- [33] L. Simonin, J.F. Colin, V. Ranieri, E. Canevet, J.F. Martin, C. Bourbon, C. Baetz, P. Strobel, L. Daniel, S. Patoux, *J. Mater. Chem.* 22 (2012) 11316–11322.
- [34] J.K. Ngala, S. Alia, A. Doble, V.M.B. Crisostomo, S.L. Suib, *Chem. Mater.* 19 (2007) 229–234.
- [35] M. Tabuchi, A. Nakashima, K. Ado, H. Sakaebe, H. Kobayashi, H. Kageyama, K. Tatsumi, Y. Kobayashi, S. Seki, A. Yamanaka, *J. Power Sources* 146 (2005) 287–293.
- [36] D. Pasero, N. Reeves, V. Pralong, A.R. West, *J. Electrochem. Soc.* 155 (2008) A282–A291.
- [37] A. Boulineau, L. Croguennec, C. Delmas, F. Weill, *Solid State Ionics* 180 (2010) 1652–1659.
- [38] A. Boulineau, L. Croguennec, C. Delmas, F. Weill, *Dalton Trans.* 41 (2012) 1574–1581.
- [39] Z.H. Chen, Y. Ren, Y. Qin, H.M. Wu, S.Q. Ma, J.G. Ren, X.M. He, Y.K. Sun, K. Amine, *J. Mater. Chem.* 21 (2011) 5604–5609.
- [40] E.R. Malinowski, *Factor Analysis in Chemistry*, Wiley, New York, 1991.
- [41] S. Valle, W.H. Li, S.J. Qin, *Ind. Eng. Chem. Res.* 38 (1999) 4389–4401.
- [42] Y. Gorlin, B. Lassalle-Kaiser, J.D. Benck, S. Gul, S.M. Webb, V.K. Yachandra, J. Yano, T.F. Jaramillo, *J. Am. Chem. Soc.* 135 (2013) 8525–8534.